Integrated Impacts of Building Space Ratio and Wind Direction on Pedestrian-level Wind Environment around High-rise Buildings with Equilateral Triangle Arrangement

H. Cui[1,2,3], M. Ma[4], J. Li [4], L. Yang [3], Z. Han[1,2,4] and Q. Liu[1,2,4†]

[1]*State Key Laboratory of Mechanical Behavior and System Safety of Traffic Engineering Structures, Shijiazhuang Tiedao University, Shijiazhuang 050043, China*
[2]*Innovation Center for Wind Engineering and Wind Energy Technology of Hebei Province, Shijiazhuang 050043, China*
[3]*Department of Mathematics and Physics, Shijiazhuang Tiedao University, Shijiazhuang 050043, China*
[4]*School of Civil Engineering, Shijiazhuang Tiedao University, Shijiazhuang 050043, China*

†Corresponding author Email: qk@stdu.edu.cn

ABSTRACT

The issue of pedestrian-level wind environments around high-rise buildings is closely related to the comfort and safety of human settlements. In this paper, we study the effects of different wind direction angles and spacing ratios on the wind environment at pedestrian heights around buildings arranged in an equilateral triangle configuration. Three-dimensional steady-state numerical simulation was employed, with the standard k-ε model selected as the turbulence model. Wind speed ratios and different area ratio parameters are used to quantitatively express the degree and range of influence of wind speed by buildings. The results show that the maximum wind speed ratio at the corner of a building is greatly affected by the wind direction angle, with 45°, 135°, and 157.5° being the unfavorable wind direction angles. Conversely, the area ratio of different areas is greatly affected by the spacing ratio. As the spacing ratio increases, the mutual interference effect between buildings weakens, resulting in a better pedestrian wind environment. Owing to the unique layout of the building group, different degrees of ventilation corridors are formed among the three buildings. The wind speed amplification effect in the corridors is more significant, and the areas with poor wind environments are concentrated in these corridors.

1. INTRODUCTION

With the continuous development of urban modernization in our country, super high-rise building groups are becoming increasingly common. The presence of these buildings significantly changes the airflow around them, creating high wind speed areas near the ground that are not conducive to normal pedestrian activities, or low wind speed areas that are not conducive to natural ventilation and the diffusion of pollutants. Stathopoulos et al. (1992) demonstrated that the knowledge-based method is suitable for the preliminary evaluation of the wind environment around buildings, which can provide valuable assistance for urban planning and architectural design. Therefore, a more in-depth study of the pedestrian wind environment around high-rise buildings is necessary to propose more effective solutions.

In recent years, scholars both domestically and internationally have conducted numerous studies on the wind environment at pedestrian heights around buildings, leading to a comprehensive understanding of the impact on individual high-rise buildings. By analyzing the wind speed distribution rules around 40 individual buildings with varying section shapes, Xiaoda et al. (2017) summarized the diverse effects of architectural form on the pedestrian-level wind environment, noting that the local projection width beneath the building significantly affects the distribution of pedestrian wind speed around the building. Hemant et al. (2018) examined the impact of various angle modification methods on the pedestrian wind environment around a single building and discovered that rounded corner modifications were the most effective at improving the pedestrian wind environment for the same degree of modification. Zhuangning et al. (2020) conducted wind tunnel tests on pedestrian-height wind

NOMENCLATURE

$A_{0.3}$	area ratio of the weak wind zone	R_{max}	variation of the maximum wind speed ratio
$A_{1.4}$	area ratio of the strong wind zone	S	cross-sectional area of the building
A_{com}	area ratio of the tolerable wind	$S_{0.3}$	area around the building where the wind speed ratio $R<0.3$
$A_{0.3,avg}$	averaged weak wind zone	$S_{1.4}$	area around the building where the wind speed ratio $R>1.4$
$A_{1.4,avg}$	averaged strong wind zone	S_{com}	area around the building where the wind speed ratio is $0.3\leq R\leq 1.4$
$A_{com,avg}$	averaged tolerable wind zone	S_T	area of the evaluation area
$A_{0.3,\theta j}$	weak wind zone $A_{0.3}$ around the building in the direction of θ_j	t	time
$A_{1.4,\theta j}$	strong wind zone $A_{1.4}$ around the building in the direction of θ_j	$u,v,$ w	average velocity components in the x, y and z directions
$A_{com,\theta j}$	tolerable wind zone A_{com} around the building in the direction of θ_j wind	U_i	average wind speed at the measuring point i of pedestrian height around the building
$C_{1\varepsilon},C_{2\varepsilon}, C_\mu$	constants in standard k-ε models	U_0	average wind speed at the pedestrian height at the entrance
D	building width	V_0	wind velocity at Z_0
G_b	turbulent kinetic energy generation term caused by buoyancy	V_z	wind speed at altitude Z
G_k	turbulent kinetic energy generation term caused by mean velocity gradient	x,y,z	dimensional coordinates
H	building height	Y_M	contribution of pulsation dissipation to dissipation rate in compressible turbulent flow
k	turbulent kinetic energy	Z,Z_0	dimensionless coordinates
L	distance between the centers of each building	α	the index considering the ground roughness
N	number of wind angles	ε	dissipation rate
p	pressure	θ	wind angle
P_i	wind tunnel test results	θ_j	building in the direction
q	credibility index	μ	fluid viscosity coefficient
Q_i	CFD simulation results	ρ	air density
R	wind speed ratio	$\sigma_k, \sigma_\varepsilon$	constants in standard k-ε models

environments within 12 meters (m) of the base area of a single square-section building and found no significant correlation between the maximum acceleration ratio and wind angle. Sadia et al. (2023) employed large eddy simulation to analyze the turbulent wake shedding process and the characteristics

of the vortex structure after high-rise and low-rise buildings with a Reynolds number of 1.2×10^4. Hassan et al. (2022) investigated the airflow around high-rise buildings with high Reynolds numbers through numerical simulation and comparison with existing wind tunnel test data, identifying different flow vorticity regions in the adjacent and distant wake streams. Jie (2010) simulated the wind environment around a single building under various overhead conditions and found that the wind speed of the overhead flow at the bottom of the building could reach about twice that, yet at a certain distance from the wake of the building, the wind speed was lower than without the overhead. Through a series of wind tunnel tests, Tsang et al. (2011) observed that, under the same conditions, wider single-story buildings adversely affected ventilation more significantly, whereas taller single-story buildings were more conducive to natural ventilation around the building. Tse et al. (2017) demonstrated that elevating buildings could maintain an ideal wind environment near these structures by adjusting their core size. In summary, previous studies indicate that

the aerodynamic shape of a building significantly influences the wind environment around it.

Concurrently, numerous scholars have initiated investigations into the pedestrian wind environment surrounding building clusters and urban-scale areas. Employing wind tunnel experiments and numerical simulation methods, Hemant et al. (2019) examined the impact of parallel, tandem, and staggered configurations between two high-rise buildings on the pedestrian wind environment, demonstrating that tandem and parallel configurations significantly influence strong wind conditions. Lian et al. (2021) conducted wind tunnel tests on the wind environment in a community following the introduction of high-rise buildings and discovered that the maximum comfort level and the probability of exceeding risk thresholds for wind conditions in the community increased by two and six times, respectively. Yi et al. (2011) utilized numerical simulations to evaluate and enhance the wind environment around high-rise buildings comprising both a new and an old building. Wenfeng et al. (2019) performed a numerical simulation study on the ambient wind environment of a building cluster under three typical layouts, finding that the outdoor wind environment of building groups with different layouts varied under different wind directions. To explore the effect of the orientation of building groups on the wind environment, Xiaoyu et al. (2018) simulated six high-rise building groups and found that the wind environment

around high-rise buildings could be optimized by altering the building orientation. Zahid Iqbal and Chan (2016) applied the stable Reynolds-averaged Navier-Stokes (RANS) method for airflow analysis and determined that increasing building spacing or adjusting building orientation appropriately could enhance the flow velocity within the accessible angle. Using wind tunnel testing, Chenggang et al. (2016) investigated the effects of surface roughness and wind direction on the wind environment around a cluster of high-rise buildings, revealing that a smaller surface roughness leads to a larger strong wind zone. Unlike individual buildings, the wind environment around a cluster of buildings is influenced not only by their aerodynamic shapes but also by their layout and spatial configuration.

Correspondingly, numerous scholars have conducted research on the numerical simulation methods for the pedestrian wind environment around high-rise buildings. Toparlar et al. (2014) compared the experimental data from high-resolution thermal infrared satellite images during the heat wave in July 2006 with computational fluid dynamics (CFD) simulations, and the results showed that CFD has the potential to accurately predict the urban microclimate. Blocken et al. (2016), through the comparison and verification of different wind tunnel tests and CFD techniques, found that low-cost wind tunnel tests and stable RANS simulations were effective in regions with a high amplification factor (>1), providing accurate results (about 10%). At low magnification factors (<1), however, the accuracy of the results decreased. Nonetheless, high magnification factors contributed most significantly to the probability of exceeding the discomfort threshold in the wind comfort criterion, indicating that the reduced accuracy in regions with low magnification factors does not necessarily undermine the accuracy of the overall wind comfort assessment. Ricci et al. (2020) discovered that in the accuracy and reliability of RANS CFD simulations for the three-dimensional stability of the urban environment, the choice of turbulence model had a greater influence than the applied surface roughness height. In summary, although large eddy simulations were more accurate, they required significantly more computational resources compared to RANS simulations. Nonetheless, more accurate data could also be derived from RANS simulations, leading to the use of 3D stable numerical simulations in this study.

To satisfy the architectural requirements for distance, lighting, and ventilation in daily life, modern super-high-rise buildings have adopted various layout forms, including juxtaposition, staggered, and enclosed configurations. Architectural clusters arranged in an equilateral triangle offer the benefits of land resource conservation and expansive views, making them a prevalent choice in urban design. However, the wind environment at pedestrian heights around these buildings has not yet been systematically investigated.

In this study, we selected three high-rise buildings arranged in an equilateral triangle within a specific layout and employed CFD for the numerical simulation of wind speed distribution at pedestrian heights around the buildings, considering various spacing ratios and wind

Table 1 Working cases

Name	Spacing ratio L/D	Wind angle θ
1	2.5	0°, 22.5°, 45°, 67.5°, 90°, 45°,112.5°, 135°, 157.5°, 180°
2	3.0	
3	3.5	
4	4.0	
5	5.0	

angles. We determined appropriate spacing ratios and orientations through quantitative evaluation and analysis of the maximum wind speed ratio and the acceleration area ratio.

2. MODEL AND NUMERICAL METHODS

2.1 Physical Model and Boundary Conditions

In this paper, we select a computational model of a 33-story building located in China as the physical model. As shown in Figure 1, the building's height H is 100 m, and its width D is 20 m. Three identical buildings form a cluster in an equilateral triangular arrangement, with the spacing ratio L/D defined, where L represents the distance between the centers of each building. Various factors influence the pedestrian wind environment around buildings arranged in an equilateral triangle. For example, variations in the inter-building spacing ratio L/D can lead to different effects on the outdoor wind field of a building group, as can the incoming flow conditions.

As shown in Table 1, this study considers five working conditions with L/D ratios of 2.5, 3.0, 3.5, 4.0, and 5.0, following the relevant architectural design codes (GB50180, 1993; GB50352, 2005; GB50016, 2014) to ensure the architectural group layout's rationality. We employ the wind direction splitting method, commonly used in meteorological studies, taking into account the model's symmetry. Wind direction θ is set to range from 0° to 180° at intervals of 22.5°, as shown in Fig. 1.

In CFD numerical simulations, to maintain the accuracy of the calculation results, the size of the calculation domain (length × width × height) is selected as $15H \times 10H \times 5H$ (Yidong et al. 2016). The boundary conditions are shown in Fig. 2. The domain inlet is set as a velocity-inlet and the outlet as outflow. The two lateral faces and the top face are symmetric boundaries. The bottom and building surfaces follow a no-slip condition. An exponential law describes the variation of wind speed with height at the velocity-inlet boundary:

$$\frac{V_z}{V_0} = \left(\frac{Z}{Z_0} \right)^{\alpha} \tag{1}$$

In the above equation, V_z is the wind speed at altitude Z, in m/s; V_0 refers to the wind velocity at reference height Z_0, in m/s. The reference height Z_0 is 10 m according to the Building Structural Load Code GB50009 (2012) and V_0 is set to 4 m/s in this paper. α is the index considering the ground roughness. Given the urban setting with dense buildings, this paper assumes a type C wind field, with α = 0.22.
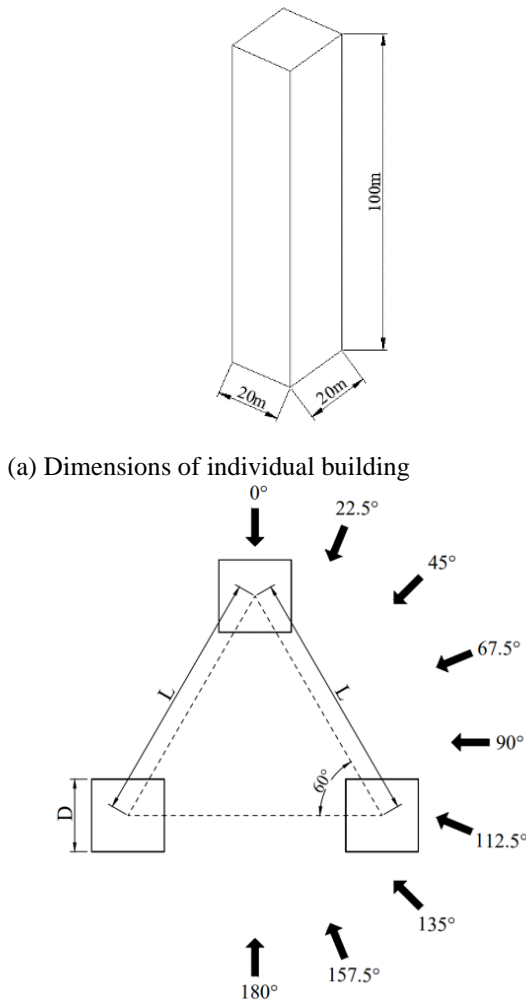
(a) Dimensions of individual building

(b) Top view of the building group

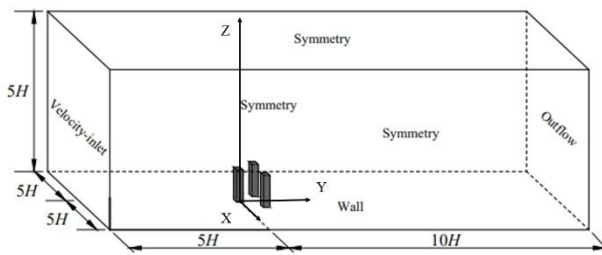**Fig. 1 Layout diagram of the building**

Fig. 2 Calculation domain and boundary conditions for the building group

2.2. Governing Equations

In CFD numerical simulations, various turbulence models exhibit distinct advantages, disadvantages, and application scopes. The selection of a turbulence model critically influences the computational results. Jie (2010) verified five different RANS turbulence models, including the standard k-ε model, RNG k-ε model, Realizable k-ε model, standard k-ω model, and SST k-ω model. These models were applied to calculate and analyze a single square-section building. The findings indicate that the standard k-ε model and the RNG k-ε model perform better in simulating the acceleration area adjacent to the

building. Considering computational efficiency, this paper employs the standard k-ε turbulence model for building simulations. The governing equations using the standard k-ε model are as follows:

Continuity equation:

$$\frac{\partial u}{\partial x} + \frac{\partial v}{\partial y} + \frac{\partial w}{\partial z} = 0 \tag{3}$$

Momentum equations:

$$\frac{\partial u}{\partial t} + u\frac{\partial u}{\partial x} + v\frac{\partial u}{\partial y} + w\frac{\partial u}{\partial z} = -\frac{1}{\rho}\frac{\partial p}{\partial x} + v'\left(\frac{\partial^2 u}{\partial x^2} + \frac{\partial^2 u}{\partial y^2} + \frac{\partial^2 u}{\partial z^2}\right) \tag{4}$$

$$\frac{\partial v}{\partial t} + u\frac{\partial v}{\partial x} + v\frac{\partial v}{\partial y} + w\frac{\partial v}{\partial z} = -\frac{1}{\rho}\frac{\partial p}{\partial y} + v'\left(\frac{\partial^2 v}{\partial x^2} + \frac{\partial^2 v}{\partial y^2} + \frac{\partial^2 v}{\partial z^2}\right) \tag{5}$$

$$\frac{\partial w}{\partial t} + u\frac{\partial w}{\partial x} + v\frac{\partial w}{\partial y} + w\frac{\partial w}{\partial z} = -\frac{1}{\rho}\frac{\partial p}{\partial z} + v'\left(\frac{\partial^2 w}{\partial x^2} + \frac{\partial^2 w}{\partial y^2} + \frac{\partial^2 w}{\partial z^2}\right) \tag{6}$$

k equation：

$$\frac{\partial}{\partial t}(\rho k) + \frac{\partial}{\partial x_i}(\rho k u_i) = \frac{\partial}{\partial x_j}\left[\left(\mu + \frac{\mu_t}{\sigma_k}\right)\frac{\partial k}{\partial x_j}\right] + G_k + G_b - \rho\varepsilon - Y_M \tag{7}$$

ε equation：

$$\frac{\partial}{\partial t}(\rho\varepsilon) + \frac{\partial}{\partial x_i}(\rho\varepsilon u_i) = \frac{\partial}{\partial x_j}\left[\left(\mu + \frac{\mu_t}{\sigma_k}\right)\frac{\partial\varepsilon}{\partial x_j}\right] + C_{1\varepsilon}\frac{\varepsilon}{k}(G_k + C_{3\varepsilon}G_b) - C_{2\varepsilon}\rho\frac{\varepsilon^2}{k} \tag{8}$$

In the above equations, u, v and w represent the average velocity components in the x, y and z directions, respectively, in m/s; t represents time, in s; p is the pressure, in Pa; ρ is the air density, in kg/m^3; μ is the fluid viscosity coefficient. G_k represents the generation term of the turbulent kinetic energy k due to the mean velocity gradient, while G_b is the production term of k due to buoyancy. Y_M accounts for the contribution of pulsational expansion in compressible turbulence. The variables k and ε are the Prandtl numbers corresponding to turbulent kinetic energy and dissipation rate, respectively. The constants in the standard k-ε models are: $C_{1\varepsilon}$=1.44, $C_{2\varepsilon}$=1.90, C_μ=0.09, σ_k=1.00 and σ_ε=1.30.

In this paper, the equations are discretized using the finite volume method. The convection term in the governing equation adopts the second-order upwind scheme. The solver utilizes an incompressible steady-state algorithm based on pressure solution. The SIMPLE method is employed to couple velocity and pressure. Monitoring points are established in the flow field and monitored. When the residuals of the continuity equations are below 10^{-6} and the wind speed values at the monitoring points in the flow field stabilize, the flow field is considered fully developed, and the simulation is deemed to have reached the convergence criterion.

2.3 Grid Independence Verification.

A partitioned structured mesh is utilized for mesh partitioning, and the building walls are refined, as shown in Fig. 3. To ensure the simulation results are unaffected by mesh quality while considering computational costs, grid independence verification is performed. Three mesh configurations with varying densities are derived by

Table 2 Different grid schemes

Grid name	Height of the first layer grid.(m)	Rate of increase	Grid quantity
Mesh 1	0.15	1.2	4,680,000
Mesh 2	0.08	1.2	6,750,000
Mesh 3	0.05	1.2	8,630,000

(a) Grids around the building group

(b) Local grids near the ground and building walls
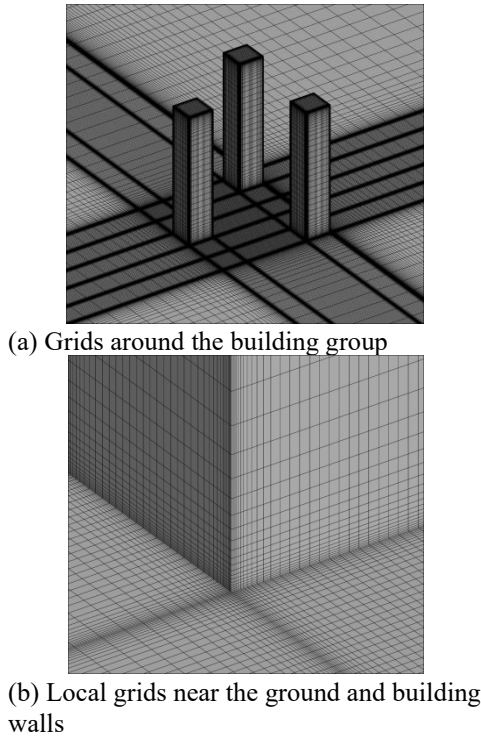
Fig. 3 Diagram of grid division

Fig. 4 Grid Independence Verification

(a)Wind tunnel test device

(b) Arrangement of measuring points (L/D=2.5)

Fig. 5 Experimental setup

adjusting the height of the first layer of the mesh. As shown in Table 2, the heights of the first layer are 0.15 m, 0.08 m, and 0.05 m, respectively, with a growth rate of 1.2 in the region near the wall.

In addition, 15 measurement points are randomly selected in the central regions of the three buildings to compare the simulation outcomes across different mesh configurations, as shown in Figure 4. Using scheme 2 as the reference, the wind speed U at the measurement points is compared in a pairwise manner with scheme 1 and scheme 3. The maximum relative error observed is 10.77%. In contrast, the discrepancy between scheme 3 and scheme 2 is minimal, with a maximum relative error of 2.1%. To achieve precise simulation outcomes with limited computing resources and time, grid scheme 2 is selected. Moreover, the difference in the mean and root mean square (RMS) values of drag and lift coefficients across different mesh configurations is also under 5.0%. There are no significant variations in induced wind profiles, such as turbulence kinetic energy (TKE), turbulence dissipation rate(TDR), and velocity.

2.4 Verification of Numerical Simulations and Wind Tunnel Tests

To verify the accuracy of the numerical simulation, a wind tunnel test was conducted with a 0° wind direction angle when the building spacing ratio is *L/D*=2.5. The experimental data were then compared with the simulation results. The wind tunnel test took place in the STU-1 wind
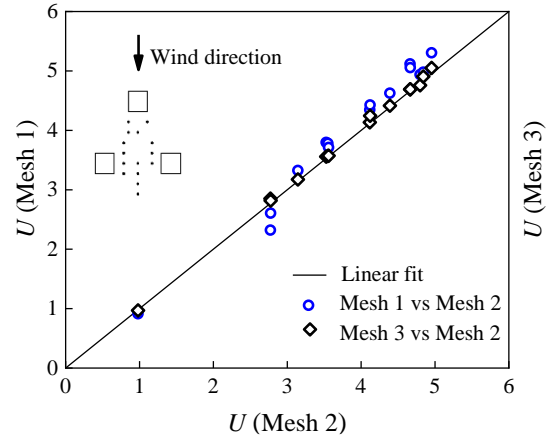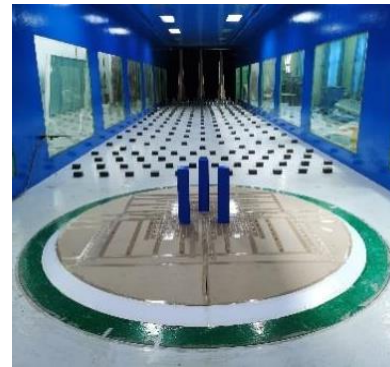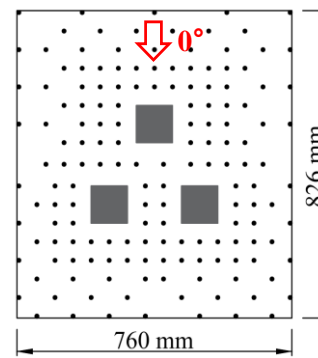
tunnel at Shijiazhuang Tiedao University. The model area in the low-speed test section measures 4.4 m in width, 3.0 m in height, and 24.0 m in length, accommodating maximum wind speeds above 30 m/s and turbulence below 0.4%. The test model setup is depicted in Figure 6. The model, constructed from acrylonitrile-butadiene-styrene (ABS) board, features a geometric scale ratio of 1:200 and a blockage ratio of less than 3%.

Figure 5 illustrates the layout of the wind tunnel test site and monitoring points. Wind speed at a pedestrian
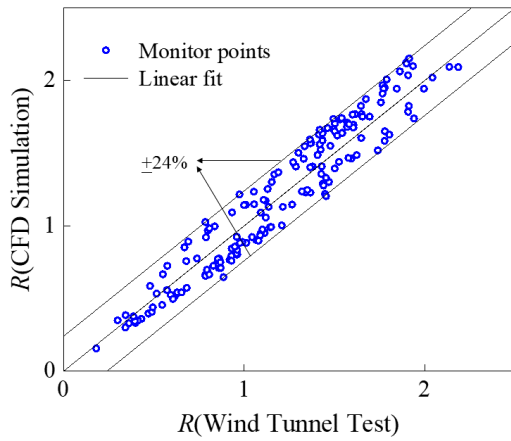
Fig. 6 Verification results of wind tunnel test and CFD simulation

height of 2 m was measured using an Irwin probe (1981), which was rigorously calibrated before the test. Wedges and rough elements were utilized to simulate the atmospheric boundary layer wind field for a Class C landform as outlined in the "Load Code for the Design of Building Structures (GB50009, 2012)". The pinhole diameter d of the probe used in this test is 0.001 m, and the horizontal and vertical spacing of the probe complies with the specified requirements (Hanqing & Stathopoulos 1994). The minimum spacing for the probe is set at 0.05 m, with the maximum spacing at 0.2 m. In total, 157 probes were deployed.

Figure 6 illustrates the comparison of test and simulation discrepancies at each measurement point for a 0° wind direction angle. The greatest margin of error, approximately 24.00%, was observed in the wake area on the leeward side of the building, while the smallest error was 2.23%. Compared with previous studies, the simulation outcomes reported in this paper demonstrate considerable accuracy and reliability.

To enhance the reliability of this numerical simulation further, the credibility index q is employed to quantitatively assess the simulation's credibility. The closer the q value is to 1, the greater the confidence in the numerical simulation outcomes. It is defined as follows:

$$q = \frac{1}{N} \sum_{i=1}^{N} n_i \tag{9}$$

$$n_i = \begin{cases} 1 & \left| \dfrac{P_i - Q_i}{P_i} \right| \leq 0.2 \text{ or } |P_i - Q_i| \leq 0.2 \\ 0 & \text{el se} \end{cases} \tag{10}$$

In the equations above, N represents the number of measurement points. P_i and Q_i denote the wind tunnel test results and CFD simulation results at the i-th measurement point, respectively. This paper sets both relative and absolute error values at 20%, considered reliable according to Bowen et al. (2021).

The q value for a wind direction angle of 0° was found to be 0.866, signifying the reliability of the numerical simulation in this study. This indicates a strong correlation

between the numerical simulation results and the experimental findings.

3. RESULTS AND DISCUSSION

3.1 Pedestrian wind Environment Evaluation Index

Currently, there is no universal evaluation criterion for assessing the pedestrian wind environment around buildings. Drawing from the research conducted in this paper, the following evaluation metrics have been selected from existing evaluation methods and criteria for the quantitative analysis of pedestrian wind environments around buildings:

(1) Wind speed ratio

The wind speed ratio R is commonly used to describe the impact of buildings on the local ambient wind speed. A value greater than one indicates an amplification of the wind speed, with larger values signifying a more pronounced effect and a higher likelihood of locally strong winds. The specific definition is as follows:

$$R = \frac{U_i}{U_0} \tag{11}$$

In the equation above, U_i is the average wind speed at the measuring point i at pedestrian height around the building (2 m above ground level, as selected for this study), m/s; U_0 is the average wind speed at pedestrian height at the entrance, m/s, in the absence of buildings. Additionally, the maximum wind speed ratio around a building is defined as the maximum wind speed ratio R_{max}.

(2) Regional wind area ratio

To quantitatively and comprehensively evaluate the pedestrian wind environment around the building group, while considering the impact of the wind speed amplification effect and the adverse ventilation phenomenon caused by the calm wind area on the leeward side of the building, wind speed ratio thresholds of $R=1.4$ for pedestrian comfort and $R=0.3$ for adverse ventilation are established. Table 3 categorizes different wind speed zones. An area with $R<0.3$ is identified as a weak wind zone, which does not support the thermal comfort needs of pedestrians during summer, nor does it facilitate natural ventilation and pollutant dispersion, leading to potential pollutant accumulation. Conversely, regions with $R>1.4$ are considered strong wind areas (Richard 1980), which can disrupt normal pedestrian activities, especially under windy conditions, where the impact may be more pronounced. As shown in Table 3, the area with $0.3 \leq R \leq 1.4$ at pedestrian height around the building is classified as a tolerable zone.

Table 3 Different wind speed zones

Name	Wind speed ratio R
Weak wind zone	$R<0.3$
Tolerable wind zone	$0.3 \leq R \leq 1.4$
Strong wind zone	$R>1.4$

Accordingly, the area ratios of the strong wind zone $A_{1.4}$, the weak wind zone $A_{0.3}$, and the tolerable wind zone A_{com} are defined as follows:

$$A_{1.4} = \frac{S_{1.4}}{S} \tag{12}$$

$$A_{0.3} = \frac{S_{0.3}}{S} \tag{13}$$

$$A_{\text{com}} = \frac{S_{\text{com}}}{S_{\text{T}}} \tag{14}$$

In the equations above, $S_{1.4}$ represents the area around the building where the wind speed ratio $R>1.4$, in m²; $S_{0.3}$ denotes the area around the building where the wind speed ratio $R<0.3$, in m²; S_{com} is the area around the building where the wind speed ratio is $0.3 \leq R \leq 1.4$, in m²; S is the cross-sectional area of the building, in m²; S_{T} is the area of the evaluation area, in m². An evaluation area of 400 m × 400 m is considered around the center of the perpendicular center of the equilateral triangle formed by the centers of each building.

(3) Average regional wind area ratio

The average strong wind zone $A_{1.4,\text{avg}}$, averaged weak wind zone $A_{0.3,\text{avg}}$, and average tolerable wind zone $A_{\text{com,avg}}$ are defined as follows:

$$A_{1.4,\text{avg}} = \frac{\sum_{j=1}^{N} A_{1.4,\theta_j}}{N} \tag{15}$$

$$A_{0.3,\text{avg}} = \frac{\sum_{j=1}^{N} A_{0.3,\theta_j}}{N} \tag{16}$$

$$A_{\text{com,avg}} = \frac{\sum_{j=1}^{N} A_{\text{com},\theta_j}}{N} \tag{17}$$

In the equations above, θ represents the wind angle; $A_{1.4,\theta_j}$ is the area of the strong wind zone $A_{1.4}$ around the building in the direction of θ_j; $A_{0.3,\theta_j}$ is the area of the weak wind zone $A_{0.3}$ around the building in the direction of θ_j; A_{com,θ_j} is the area of the tolerable wind zone A_{com} around the building in the direction of wind θ_j; N is the number of wind angles.

3.2 Influence of Wind Angle and Spacing Ratio on Wind Speed Ratio

Figure 7 shows the contours of the wind speed ratio at a pedestrian height of 2 m around the building for various wind directions with spacing ratio L/D=2.5. Different acceleration and deceleration zones emerge around the building for varying wind directions, underscoring the significant impact of wind direction on the distribution of the wind field at pedestrian heights within the building group. At wind angles of 0° and 180°, the flow field is symmetrically distributed, with the buildings significantly obstructing the airflow, thereby creating a large area of strong wind outside the buildings. It is crucial to recognize that, owing to the unique pin-shaped layout, the interior of the three buildings forms corridors with varying degrees of ventilation. Due to the "venturi effect," the wind speed amplification in these
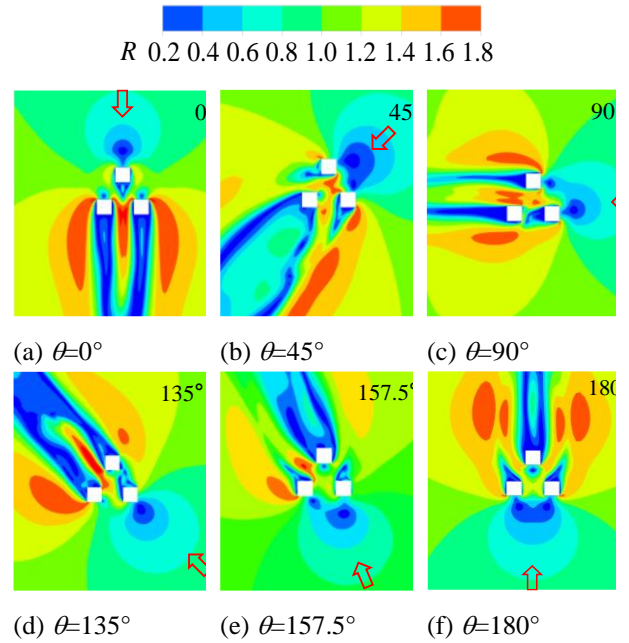

(a) θ=0°   (b) θ=45°   (c) θ=90°

(d) θ=135°   (e) θ=157.5°   (f) θ=180°

Fig. 7 Cloud image of the wind speed ratio distribution at a pedestrian height of 2 m around the building group at L/D=2.5
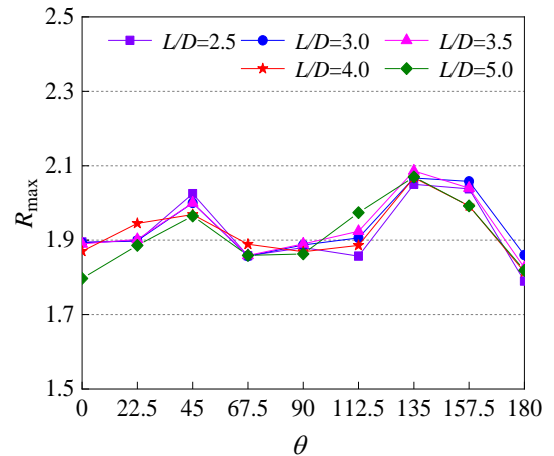

Fig. 8 Variation of the maximum wind speed ratio $R_{\max}$ with the wind angle q of the building group

areas is particularly pronounced at wind angles of 0°, 90°, and 135°.

From Fig. 8, it is observed that $R_{\max}$ occurs at the corners on both sides of the building, where significant vortex separation takes place. Building-induced wind amplification was most notable, leading to locally strong winds. Figure 8 also illustrates how $R_{\max}$ varies with the wind direction angle for different spacing ratios. The trend of $R_{\max}$ under various operational conditions generally remains consistent with the change in wind angle, fluctuating between 1.8 and 2.1. This indicates that variations in the wind direction angle impact $R_{\max}$ at pedestrian heights around the buildings to a certain degree. With changes in wind direction angle, two intervals of sudden increase are noted, resulting in three pronounced peaks, which occur at oblique wind directions of 45°, 135°, and 157.5°. The corresponding maximum values of
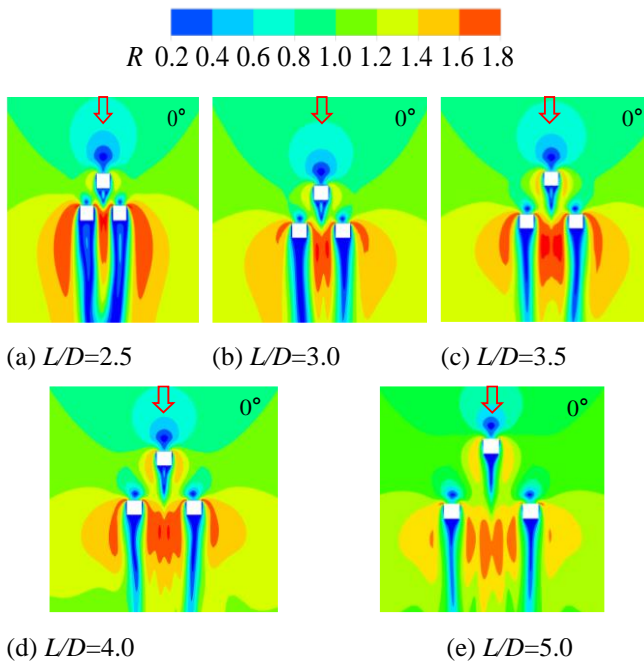
(a) *L/D*=2.5   (b) *L/D*=3.0   (c) *L/D*=3.5

(d) *L/D*=4.0   (e) *L/D*=5.0

Fig. 9 Distribution cloud map of pedestrian height around buildings with wind direction of 0°

R_{max} are 2.03 (*L/D*=2.5), 2.09 (*L/D*=3.5), and 2.06 (*L/D*=3.0), respectively. The alteration in wind angle gradually accentuates sharp corners in the building group, intensifying corner winds and thereby increasing R_{max}. Conversely, the variation of the maximum wind speed in relation to R_{max} is less pronounced at other wind direction angles.

Figure 9 illustrates the distribution of pedestrian height and wind speed ratio around a group of buildings with varying spacing ratios at a 0° wind angle. The flow that bypasses the upstream building splits into two parts: one flows directly through the channel formed by the two parallel downstream buildings, while the other encounters an obstruction from the downstream building, causing the flow to resume. When the spacing is relatively small, the building group behaves more like a single large building, allowing only a small fraction of the accelerated flow to bypass the upstream building and enter the downstream channel. Most of the flow combines with the incoming wind on the windward side of the downstream building, accelerating and backflowing outward, which results in a large area of strong winds on the exterior of the downstream building. As the spacing ratio increases, the flow field around the upstream buildings gradually develops. Most of the accelerated flow bypassing the upstream buildings flows into the downstream channel, significantly reducing the area of strong winds outside the downstream buildings. Changes in the low wind speed region are primarily due to the effects of the building wake. The smaller the spacing ratio, the more the wake region behind the downstream building connects, creating a larger calm wind region.

Figure 10 shows the variation of the maximum wind speed ratio R_{max} with the spacing ratio *L/D* at pedestrian height around the building. Considering various wind directions and in the range of *L/D* from 2.5 to 5.0, R_{max}
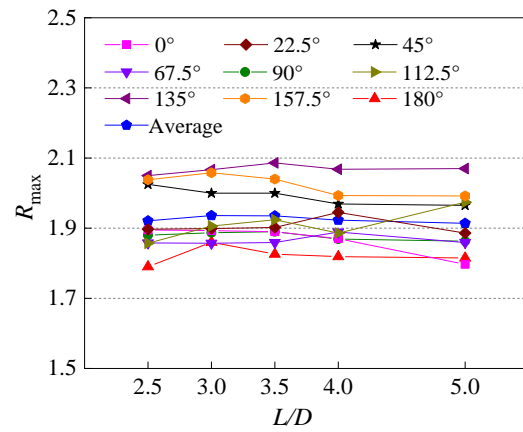

Fig. 10 Variation of the maximum wind speed ratio R_{max} with the building spacing ratio *L/D* of the building group

varies minimally with the spacing ratio, within 5%; the average value of R_{max} remains approximately 1.93. This indicates that R_{max} is less influenced by the building spacing ratio *L/D* compared to the wind direction. A change in wind angle, notably the formation of sharp corners in the building group, significantly impacts R_{max}.

3.3 Influence of Wind Angle on Regional Wind Area Ratio

Figure 11 shows the area ratio of the strong wind zone $A_{1.4}$ for various wind directions under different operational conditions. The figure reveals that the area ratio of the strong wind zone $A_{1.4}$ significantly changes as the wind direction angle varies. The discussion is categorized based on the differences in the spacing ratio. The trend of variability for $A_{1.4}$ at spacing ratios *L/D*=2.5 and 3.0 is generally consistent. Within the range of 0° to 180°, the unfavorable wind direction angles are identified as 67.5° and 180°, with the corresponding maximum values of $A_{1.4}$ being 16.30 (*L/D*=2.5) and 17.18 (*L/D*=3.0), respectively. However, $A_{1.4}$ slightly decreases at a wind direction angle of 157.5°, while under other operational conditions, $A_{1.4}$ is less impacted by wind direction, showing less significant
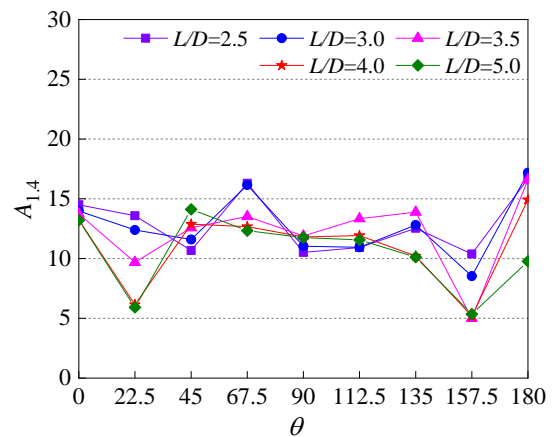

Fig. 11 Variation of the area ratio of the strong wind zone $A_{1.4}$ with the wind angle *q* of the building group

changes. The variation trend of $A_{1.4}$ at spacing ratios of L/D=3.5, 4.0, and 5.0 is generally consistent, displaying a "W" shaped change. The two lower values at the bottom of this valley occur at wind angles of 22.5° and 157.5°, which are considered favorable wind angles. The minimum values are 5.91 (L/D=5.0) and 5.00 (L/D=3.5), with the variation of $A_{1.4}$ being less significant at other wind directions.

An optimal pedestrian wind environment around buildings requires consideration of both the harm caused by wind speed amplification and the adverse effects of calm wind areas on ventilation on the leeward side of the building. Figure 12 illustrates how the area ratio $A_{0.3}$ of the weak wind zone varies with the wind direction angle. Changes in wind direction significantly affect the extent of the weak wind zone at pedestrian heights around the building. The discussion is categorized into two segments. For spacing ratios of L/D=2.5 or 3.0, the variation pattern of $A_{0.3}$ is not pronounced. The most unfavorable wind direction angle is 135°, with a maximum value of $A_{0.3}$ reaching 4.88 (L/D=2.5). For spacing ratios of L/D=3.5, 4.0, and 5.0, $A_{0.3}$ noticeably increases at wind angles of 22.5° and 157.5°. The most unfavorable wind angle is 157.5°, with the maximum value of $A_{0.3}$ being 5.20 (L/D=4.0). In other wind directions, variations in $A_{0.3}$ are less significant.
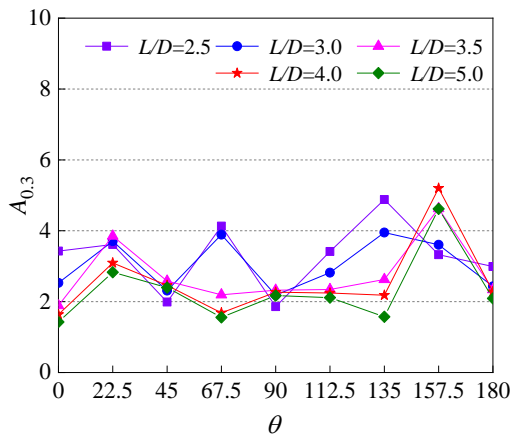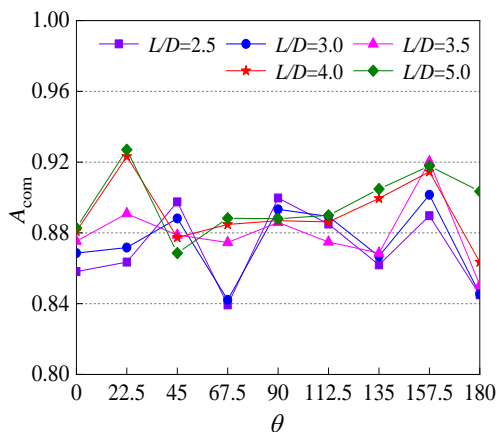
Figure 13 shows the variation of the area ratio of the tolerable wind zone at pedestrian height around the building with the wind angle. For spacing ratios of L/D=2.5 or 3.0, the fluctuation range of A_{com} is minimal, and the most unfavorable wind direction angle is 67.5°, with a minimum value of 0.84 (L/D=2.5). For spacing ratios of L/D=3.5, 4.0, and 5.0, the most favorable wind direction angle is 22.5°, with a maximum value of 0.93 (L/D=5.0).

3.4 Effect of Spacing Ratio on Regional Wind Area Ration

The impact of wind direction on the pedestrian wind environment around the buildings reveals that the wind environment generally exhibits favorable conditions when the wind angle is 0°. Subsequently, the distribution of wind fields with different spacing ratios in the downwind direction is analyzed to identify the optimal spacing ratio for buildings arranged in an equilateral triangle.

Figure 14 presents the distribution laws of $A_{1.4}$, $A_{0.3}$, and A_{com} around the building at a 0° wind angle. It is observed that $A_{1.4}$ and $A_{0.3}$ exhibit a continuous decline with an increasing spacing ratio, whereas A_{com} gradually increases until it plateaus. For the pedestrian wind environment around a building, the most unfavorable spacing ratio is identified as 2.5.
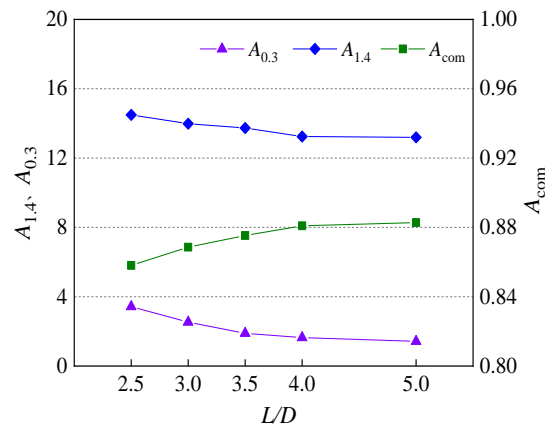

Fig. 12 Variation of the weak wind zone ratio $A_{0.3}$ with the wind direction q of the building group

Fig. 14 Variation of various wind area ratios with spacing ratios at q=0° of the building group

Fig. 13 Variation of the area ratio of the strong wind zone $A_{1.4}$ with the wind angle q of the building group

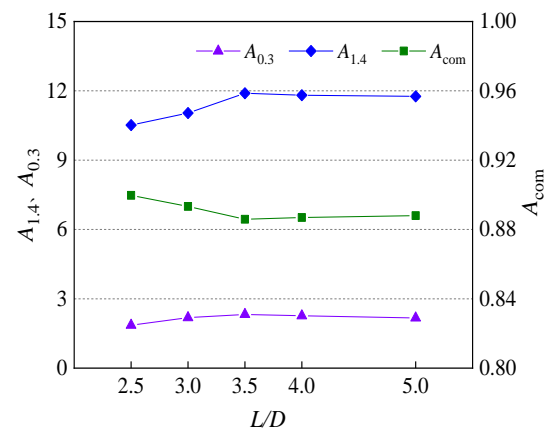**Fig. 15 Variation of wind area ratio with spacing ratio at q=90° of the building group**

Figure 15 shows the distribution of $A_{1.4}$, $A_{0.3}$ and A_{com} around the building at a 90° wind angle. It can be noted that with changes in the spacing ratio, the variation in the area ratio of the weak wind zone $A_{0.3}$ is not pronounced, the area ratio of the strong wind zone $A_{1.4}$ initially increases until it stabilizes, and the area ratio of the tolerable wind zone A_{com} first decreases until it becomes gradual.

Figure 16 shows the distribution of wind area ratios $A_{1.4}$, $A_{0.3}$ and A_{com} around the building at $q=180°$. Initially, $A_{1.4}$ increases and then decreases as the spacing ratio L/D increases, reaching its maximum value under the operational condition when the spacing ratio $L/D=3.0$. $A_{0.3}$ exhibits a continuous decreasing trend, while A_{com} gradually increases. After the air flows past the front building, the accelerated airflow in the channel encounters the obstruction of the rear building and is expelled to both sides, enhancing the angular separation effect. With the increase in the spacing ratio L/D, the flow field around the downstream buildings fully develops. The strong wind areas on both sides converge with the accelerated airflow on both sides of the upstream buildings, causing the maximum value when the spacing ratio $L/D=3$ to gradually reduce as the interference between buildings weakens. The weak wind area on the leeward side of the rear buildings also decreases.

The wind field around the building is analyzed in conjunction with each wind direction. Figure 17 illustrates the distribution of the average area-to-wind ratios $A_{1.4,avg}$, $A_{0.3,avg}$ and $A_{com,avg}$ for each spacing ratio across all wind directions. As the spacing ratio increases, $A_{1.4,avg}$ and $A_{0.3,avg}$ exhibit a continuous downward trend. Correspondingly, $A_{com,avg}$ is continuously increasing.

Overall, the spacing ratio L/D of buildings arranged in an equilateral triangle has a smaller effect on the maximum wind speed ratio R_{max} around the building but a more pronounced effect on the wind area ratio around the building. When there are no restrictions on building planning land, the larger the building spacing ratio, the better the surrounding pedestrian wind environment.

4. CONCLUSION

In this paper, we employ CFD numerical simulation methods to investigate the impact of wind angle and spacing ratio on the wind environment at pedestrian heights around buildings arranged in equilateral triangles. The following conclusions can be drawn:

(1) The maximum wind speed ratio R_{max} occurs at the corners on both sides of the building, and the spacing ratio of the building group has a minor effect on R_{max}.

(2) The impact of the wind angle on the maximum wind speed ratio R_{max} around the building group is significant. The adverse wind directions are predominantly at the downwind angles of 45°, 135°, and 157.5°. At the same spacing ratio, the R_{max} value in the downwind direction ($q=0°$) is substantially lower than in the oblique wind direction. It is advisable to avoid the aforementioned adverse wind angles for such buildings.
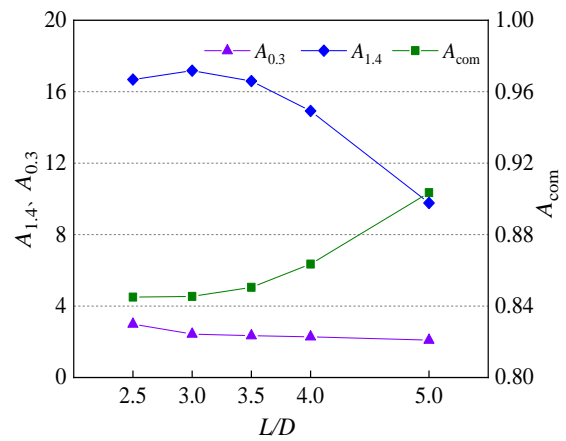

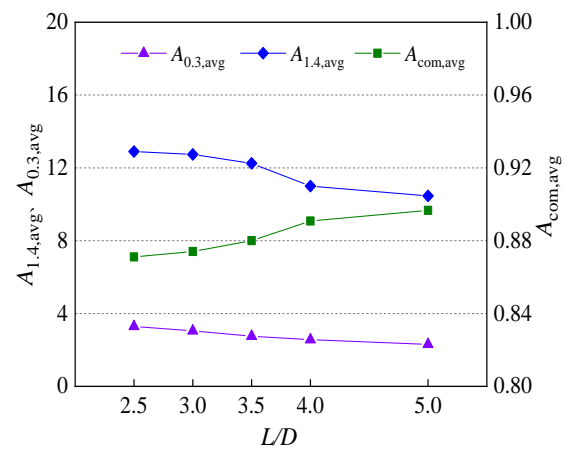**Fig. 16 Variation of wind area ratio with spacing ratio at $q=90°$ of the building group**

Fig. 17 Variation of average regional wind area ratios $A_{1.4,avg}$, $A_{0.3,avg}$ and $A_{com,avg}$ with spacing ratio L/D of the building group

(3) The building spacing ratio L/D significantly affects the wind area ratio around buildings arranged in equilateral triangles. The less favorable spacing ratios are 2.5 at a 0° wind direction, 3.5 at a 90° wind direction, and 3.0 at a 180° wind direction. As the spacing ratio increases, the area ratios of strong and weak winds around the building gradually decrease, whereas the corresponding area ratio of comfortable winds gradually increases.

(4) When land resources are scarce, to ensure the comfort and safety of pedestrians in daily activity areas, architectural designs with spacing ratios of 2.5, 3.5, and 3.0 should be avoided as much as possible at 0°, 90°, and 180° wind angles.

The findings of this paper provide a foundation for further understanding the flow field distribution around the building group and offer suggestions for optimizing adverse wind conditions. This contributes to identifying the best arrangement and the most effective optimization strategies for such buildings and offers theoretical guidance for future urban construction planning.

CONFLICTS OF INTERESTS

The authors declare that they have no known competing financial interests or personal relationships that could have appeared to influence the work reported in this paper.

AUTHORS CONTRIBUTION

Huimin Cui: Methodology, Visualization. **Mixue Ma:** Methodology, Data curation, Writing-Original draft, Writing-Reviewing and Editing. **Jiahui Li:** Writing-Reviewing and Editing. **Lingyu Yang:** Writing-Reviewing and Editing. **Zhiming Han:** Validation, Formal analysis, Resources. **Qingkuan Liu:** Resources, Supervision, Project administration.

DATA AVAILABILITY

Data will be made available on request.

REFERENCES

American Society of Heating, Refrigeration and Air-Conditioning Engineers (2005). ASHRAEF undamentals Handbook, SIED, Atlanta, USA.

Blocken, B., Stathopoulos, T., & Van Beeck, J. P. A. J. (2016). Pedestrian-level wind conditions around buildings: review of wind-tunnel and CFD techniques and their accuracy for wind comfort assessment. *Building and Environment*, *100*, 50–81. https://doi.org/10.1016/j.buildenv.2016.02.004.

Bowen, Y., Min, W., Qiao, Y., Yong, C., Zhenru, S., Qiusheng, L., & Xvhong, Z. (2021). Study on effects of tall building shape and layout on pedestrian-level wind environment in the urban area. *Journal of Hunan University Natural Sciences*, *11*, 61-71. (in Chinese). https://doi.org/10.16339/j.cnki.hdxbzkb.2021.11.007.

Chenggang, W., Feng, L., Yongwei, W., & Hongnian, L. (2016). Experimental study of the impact of high-density building clusters and high-rise buildingon the wind environment. *Transactions of Atmospheric Sciences*, *39*(01), 133-139. (in Chinese). https://doi.org/10. 13878 /j. cnki. dqkxxb. 20130107001

GB50009. (2012). *Load code for the design of building structures.* China Architecture Industry Press Beijing, Chinese.

GB50016. (2014). *Code for fire protection design of buildings.* China Planning Press Beijing, Chinese.

GB50180. (1993). *Code of urban residential district planning & design.* China Planning Press Beijing, Chinese.

GB50352. (2005). *Code for design of civil buildings.* China Planning Press Beijing, Chinese.

Hanqing, W., & Stathopoulos. T. (1994). Further experiments on Irwin's surface wind sensor. *Journal of Wind Engineering and Industrial Aerodynamics*, 53(3). 441-452. https://doi.org/10.1016/0167-6105(94)90095-7

Hassan, S., Molla, M. M., Nag, P., Akter, N., & Khan, A. (2022). Unsteady RANS simulation of wind flow around a building shape obstacle. *Building Simulation*, *15*, 291–312. https://doi.org/10.1007/s12273-021-0785-8.

Hemant, M., Ashutosh, S., & Ajay, G. (2018). Numerical simulation of pedestrian level wind flow around buildings: Effect of corner modification and orientation. *Journal of Building Engineering*, *22*, 314-326. https://doi.org/10.1016/j.jobe.2018.12.014

Hemant, M., Ashutosh, S., & Ajay, G. (2019). Investigation of pedestrian-level wind environment near two high-rise buildings in different arrangements. *Advances in Structural Engineering*, *22*(12), 2620-2634. https://doi.org/10.1177/1369433219849832

Irwin, A. (1981). simple omnidirectional sensor for wind-tunnel studies of pedestrian-level winds. *Journal of Wind Engineering and Industrial Aerodynamics*, *7*(3), 219-239. https://doi.org/10.1016/0167-6105(81)90051-9

Jie, Q. (2010). *Research on wind environment characteristics of building bottom aerial* [Master Thesis, Chongqing University], Chongqing.

Lian, S., Chunchao, T., Yan, H., Kuo, W., Chunguang, L., & Chunsheng, C. (2021). Experimental study on urban wind environment influenced byadjacent hing-rise building. *Journal of Civil and Environmental Engineering*, *43*(06), 103-112. (in Chinese). https://doi.org/10.11835/j.issn.2096-6717.2020.127

Ricci, A., Kalkman I., Blocken B., Burlando M., & Repetto M.P. (2020). Impact of turbulence models and roughness height in 3D steady RANS simulations of wind flow in an urban environment. *Building and Environment*, *171*. https://doi.org/10.1016/j.buildenv.2019.106617.

Richard, A. (1980). Politics of pedestrian level urban wind control. *Building and Environment,* (24), 291-295. https://doi.org/10.1016/0360-1323(89)90022-X

Sadia, S., Sahrish, B. N., Muhammad, A., & Molla, M. M. (2023). Large-eddy simulation of airflow dynamics around a cluster of buildings. *Proceedings of the Institution of Mechanical Engineers, Part C: Journal*

of Mechanical Engineering Science. https://doi:10.1177/09544062231172666.

Stathopoulos, T., Wu, H., & Bedard, C. (1992). Wind environment around buildings: a knowledge-based approach. *Journal of Wind Engineering & Industrial Aerodynamics*, *44*, 2377–2388. https://doi.org/10.1016/0167-6105(92)90028-9.

Toparlar, Y., Blocken, B., Vos, P., Van Heijst, G. J. F., Janssen, W. D., Van Hooff, T., Montazeri, H., & Timmermans, H. J. P. (2014). CFD simulation and validation of urban microclimate: a case study for Bergpolder Zuid, Rotterdam. *Building and Environment*, *83*, 79–90. https://doi.org/10.1016/j.buildenv.2014.08.004.

Tsang, C. W., Kwok, K. C. S., & Hitchcock, P. A. (2011). Wind tunnel study of pedestrian level wind environment around tall buildings: Effects of building dimensions, separation and podium. *Building and Environment*, *49*, 167-181. https://doi.org/10.1016/j.buildenv.2011.08.014

Tse, K. T., Xuelin, Z., Weerasuriya, A. U., Li, S. W., Kwok, K. C. S., Mak, C. M., & Niu, J. (2017). Adopting 'lift-up' building design to improve the surrounding pedestrian-level wind environment. *Building and Environment*, *117*, 154–165. https://doi.org/10.1016/j.buildenv.2017.03.011.

Wenfeng, H., Tong, Z., & Xing, C. (2019). Wind environment assessment of typical building grous by using CFD numerical simulation. *Journal of Hefei University of Technology (Natural Science)*, *42*(03), 415-421. (in Chinese) https://doi.org/10.3969/j.issn.10035060.2019.03.019.

Xiaoda, X., Qingshan, Y., Akihito, Y., & Yukio, T. (2017). Characteristics of pedestrian-level wind around super-tall buildings with various configurations.

Journal of Wind Engineering & Industrial Aerodynamics, *166*, 61-73. https://doi.org/10.1016/j.jweia.2017.03.013

Xiaoyu, Y., Rin, X., Kan, Q., & Grace, D. (2018). Design analysis of hing-rise buildings in the view of wind environment—A case study of four seasons green block in Hangzhou Qianjiang new city. *Journal of Xi'an University of Architecture & Technology (Natural Science)*, *50*(06), 884-889+900. (in Chinese). https://doi.org/10.15986/j.1006-7930.2018.06.018

Yi, Y., Xinyang, J., Liguo, Y., Hai, J., Ming, X., & Zongyi, Z. (2011). Numerical simulation research on pedestrian wind environment and optimization design of high-rise buildings. *Building Science*, *27*(01), 4-8. (in Chinese). https://doi.org/10.13614/j.cnki.111962/tu.2011.01.008

Yidong, H., Zhuang, Z., & Yuanbo, Y. (2016). Sensitivity analysis of key points of green building wind environment simulation technology. *Building Science*, *32*(08), 712+32. https://doi.org/10.13614/j.cnki.111962/tu.2016.08.02.

Zahid Iqbal, Q. M., & Chan, A. L. S. (2016). Pedestrian level wind environment assessment around group of high-rise cross-shaped buildings: effect of building shape, separation and orientation. *Building and Environment*, *101*, 45–63. https://doi.org/10.1016/j.buildenv.2016.02.015.

Zhuangning, X., Yu, L., & Xianfeng, Y. (2020). Experimental investigation on pedestrian-level wind environment around a hing-rise building. *Journal of Tongji University (Natural Science)*, *48*(12), 1726-1732. (in Chinese) https://doi.org/10.11908/j.issn.0253-374x.20197